CHEMISTRY OF MATERIALS

pubs.acs.org/cm Article

Thermal Atomic Layer Etching of Nickel Using Sequential Chlorination and Ligand-Addition Reactions

Jessica A. Murdzek, Ann Lii-Rosales, and Steven M. George*

Cite This: *Chem. Mater.* 2021, 33, 9174–9183 Read Online

ACCESS | Metrics & More | Article Recommendations

ABSTRACT: The thermal atomic layer etching (ALE) of nickel was demonstrated using sequential chlorination and ligand-addition reactions. Nickel chlorination was achieved using SO_2Cl_2 (sulfuryl chloride) as the chlorine reactant. PMe_3 (trimethylphosphine) was employed as the ligand-addition reactant. Sequential exposures of SO_2Cl_2 and PMe_3 led to Ni thermal ALE. This procedure was inspired by the covalent bond classification (CBC) method that categorizes the most common compounds of various metals. Based on the CBC method, the surface reactions during thermal Ni ALE were performed to form NiX_2L_2 products, where Cl is the X ligand and PMe_3 is the L ligand. Using this strategy, thermal Ni ALE was observed at temperatures from 75−200 °C. The etch rates were determined from in situ quartz crystal microbalance (QCM) measurements. The average etch rates determined from the mass changes were 0.14 ± 0.13, 0.57 ± 0.36, 0.67 ± 0.45, 1.30 ± 0.68, and 3.07 ± 1.56 Å/cycle for the temperatures 75, 100, 125, 150, and 175 °C, respectively. The QCM investigations revealed that there was a mass increase on every SO_2Cl_2 exposure and a mass loss on every PMe_3 exposure, resulting in a net mass loss. The amount of chlorination for a given SO_2Cl_2 exposure increased with increasing temperature. The amount of mass lost on each PMe_3 exposure also increased with increasing temperature. The etch rates were also confirmed using ex situ X-ray reflectivity measurements on Ni films on silicon wafers. The etch rates varied from 0.39 ± 0.10 Å/cycle at 125 °C to 2.16 ± 0.47 Å/cycle at 200 °C. Mass spectrometry analysis revealed that the volatile etch product was $NiCl_2(PMe_3)_2$ as expected from the CBC method. In addition, scanning electron microscopy revealed that the nickel surface morphology had negligible changes after ALE. Atomic force microscopy analysis showed that thin nickel films remained smooth during initial etching and may experience some slight roughening with progressive etching. Using the CBC method to create novel thermal ALE procedures can be generalized for the thermal ALE of many different metals.

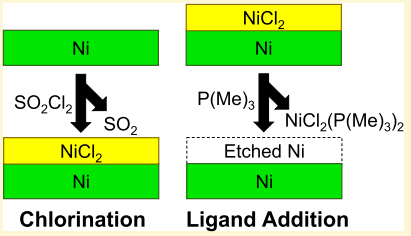

1. INTRODUCTION

Thermal atomic layer etching (ALE) is defined by sequential surface modification and volatile release reactions.[1,2] Thermal ALE can be viewed as the opposite of atomic layer deposition (ALD).[3,4] In both ALD and thermal ALE, reactants are exposed sequentially to the surface.[1−4] During thermal ALE, the surface modification step involves a reaction that changes the surface layer.[1,2] The removal step then utilizes a precursor that will create stable, volatile species when exposed to the modified surface. Because thermal ALE involves reactions with gas-phase species, thermal ALE produces isotropic etching.[5,6] Thermal ALE complements plasma ALE techniques that employ energetic ions or neutral species for the release of the etch products through sputtering and produce anisotropic etching.[7]

One possible thermal ALE mechanism involves fluorination and ligand-exchange reactions.[2,8,9] This mechanism has been used to etch a variety of metal oxides such as Al_2O_3, HfO_2, and ZrO_2.[5,9−16] Other thermal ALE pathways are possible using conversion reactions that convert the initial material to a different material.[17] These conversion reactions have facilitated the etching of various materials such as SiO_2 and WO_3.[18,19] Oxidation reactions, sometimes together with conversion reactions, have also been employed for the etching of a variety of materials such as W, TiN, Si, Si_3N_4, and SiGe.[19−23] Many thermal ALE mechanisms have been established over the last 5 years.[2]

One key group of materials that has not received as much attention is elemental metals. There has been previous work on W, Cu, and Co thermal ALE.[19,24−26] However, there are not general guidelines on procedures to volatilize metal complexes originating from elemental metals. Thermal metal ALE is particularly challenging because the oxidation state of the initial elemental metal must be changed to match the oxidation state of the volatile metal etch product. After changing the oxidation state, the metal then needs to form a stable and volatile complex.

Received: August 3, 2021
Revised: November 12, 2021
Published: December 1, 2021

In this work, thermal Ni ALE is developed by first changing the Ni oxidation state by chlorination using SO_2Cl_2. Subsequently, Ni is etched by the binding of PMe_3 ligands that can volatilize the nickel chloride. One possible volatile etch product is $NiCl_2(PMe_3)_2$. A schematic of these surface modification and volatile release reactions for thermal Ni ALE is shown in Figure 1.

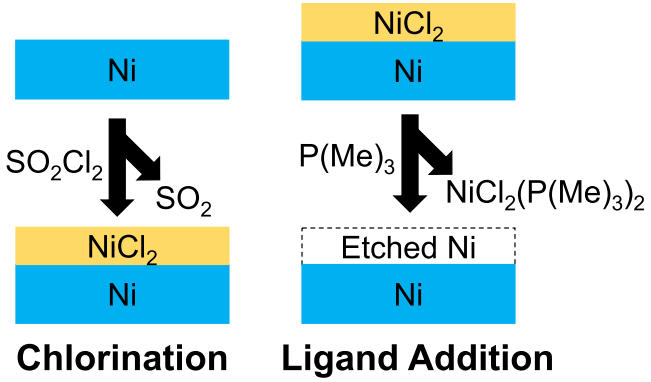

Figure 1. Proposed mechanism for nickel ALE using SO_2Cl_2 for chlorination and PMe_3 for ligand addition.

The logic of this etching approach is based on the covalent bond classification (CBC) method.[27] The CBC method classifies possible metal complexes in terms of their valence number and electron number. Various metal complexes are defined in terms of their X, L, and Z ligands.[27] X ligands are one-electron donors like Cl. L ligands are two-electron donors like PMe_3. Z ligands are two-electron acceptors like BF_3. The CBC method then assesses the probability of occurrence of various $ML_aX_bZ_c$ complexes based on all known metal complexes reported in the *Dictionary of Organometallic Complexes*.[28] The various $ML_aX_bZ_c$ complexes and their probability of occurrence are given in MLX plots.

Figure 2 displays the MLX plot for Ni. According to the CBC method, the most likely Ni complexes typically have NiL_2X_2 (33%) or NiL_3X_2 (26%) configurations. These configurations also represent metal complexes that obey the 18 or 16 electron rule. Based on the MLX plot, the goal for Ni ALE is to create volatile nickel compounds that are either NiL_2X_2 or NiL_3X_2 formed by sequential SO_2Cl_2 and PMe_3 surface reactions. The proposed surface chemistry for Ni ALE in Figure 1 assumes that SO_2Cl_2 exposure leads to $NiCl_2$ formation on the Ni substrate. The reaction of nickel with SO_2Cl_2 to form $NiCl_2$ according to $Ni + SO_2Cl_2(g) \rightarrow NiCl_2 + SO_2(g)$ is known to be thermodynamically favorable at all reaction temperatures.[29] Then, the $NiCl_2$ is volatilized by binding with PMe_3 to form either $NiCl_2(PMe_3)_3$ or $NiCl_2(PMe_3)_2$.

Other approaches have also been employed for etching nickel. Wet solution chemistry using an oxidizer, such as H_2O_2, and HF or HCl for dissolution of the oxidized nickel can be used to etch nickel.[30,31] A 30% $FeCl_3$ solution can also be used to remove nickel. The difficulty with wet solution methods is that the etch rates can be rapid at 20 nm or more per minute and cannot precisely remove at the atomic scale.[30,31] Plasma etching is another method to remove nickel. Plasma etching can be highly anisotropic and produces directional etching. Some plasma methods use Cl_2/Ar plasma and yield high etch rates between 200 and 850 Å/min.[32] A different nickel plasma etching approach used CO and NH_3 plasma and observed etch rates of 450−1300 Å/min.[33]

Other plasma etch methods for nickel involve sequential doses of reactants to control the etch rate. One sequential plasma process used Cl_2 plasma to form $NiCl_2$ and then H_2 plasma to produce gaseous nickel hydride.[34] The etch rate observed for nickel under the Cl_2 and H_2 plasma conditions was 57 Å/cycle.[34] A hybrid technique involving reactive-ion etching and ALE has also been shown to remove nickel.[35,36] The nickel ALE process used oxygen plasma to create an oxidized NiO surface. Subsequently, an exposure to formic acid for 1 h removed the oxidized nickel and produced a Ni etch rate of 6 nm/cycle.[36]

2. EXPERIMENTAL SECTION

2.1. Reactor and In Situ QCM Measurements. Thermal ALE experiments were performed in a viscous flow reactor.[37] The reaction temperatures were maintained using a proportional−integral−derivative temperature controller (2604, Eurotherm). A constant flow of pre-purified Ar gas was employed as the carrier and purge gas using mass flow controllers (type 1179A, MKS). A mechanical pump (Pascal 2015SD, Alcatel) was attached at the back of the reactor. The reactor pressure with flowing Ar carrier gas was 1 Torr. This pressure was measured using a capacitance manometer (Baratron 121A, MKS).

Each reagent was dosed into the constant stream of Ar carrier gas. The chlorination precursor was sulfuryl chloride (SO_2Cl_2, 97%,

Ni		Electron Number								
		12	13	14	15	16	17	18	19	20
Valence Number	0	ML <1%		ML_2 1%		ML_3 14%		ML_4 16%		ML_5 <1%
	1		MLX		ML_2X		ML_3X <1%		ML_4X <1%	
	2	MX_2 <1%		MLX_2 <1%		ML_2X_2 33%		ML_3X_2 26%		ML_4X_2 3%
	3		MX_3		MLX_3		ML_2X_3 <1%		ML_3X_3 <1%	
	4	MX_2Z		MX_4		MLX_4 <1%		ML_2X_4 4%		ML_3X_4 <1%

Figure 2. MLX plot for nickel.

https://doi.org/10.1021/acs.chemmater.1c02684
Chem. Mater. 2021, 33, 9174−9183

Sigma-Aldrich). The pressure transients for SO_2Cl_2 were 100 mTorr, maintained using a metering valve (SS-4BMG, Swagelok). Sulfuryl chloride decomposes to Cl_2 and SO_2 and is commonly used as a source of Cl_2.[38] The ligand-addition precursor was trimethyl phosphine (PMe_3, 97%, Sigma-Aldrich). Pressure transients for PMe_3 were 300 mTorr, maintained using a metering valve.

Quartz crystal microbalance (QCM) studies were performed in the viscous flow reactor.[37] The quartz crystals (polished, RC cut, 6 MHz, Phillip Technologies) were coated with ~2000 Å of nickel deposited by electron beam evaporation. The electron beam evaporation produced high quality, polycrystalline nickel. The nickel-coated crystal was placed in a sensor head (Inficon) and sealed with a high-temperature silver epoxy (Epo-Tek H21D, Epoxy Technology Inc.).

The QCM head was placed in an isothermal region of the reactor. A constant argon gas flow on the back of the QCM was used to prevent deposition of precursors on the backside of the QCM crystal.[37] The changes in resonant frequency of the quartz crystal were recorded and converted to mass using a thin-film deposition monitor (Maxtek TM-400, Inficon). The QCM has a precision of ~1 ng/cm^2. The nickel-coated crystal was left in the reactor at temperature to equilibrate for 12 h before starting experiments.

2.2. Ni Films for Ex Situ XRR Experiments. Nickel thin films were also employed that were prepared by Intel using physical vapor deposition on thermal SiO_2 on a silicon substrate. These nickel films were polycrystalline with a cubic structure as verified with grazing incidence X-ray diffraction (GI-XRD). Figure 3 shows the GI-XRD

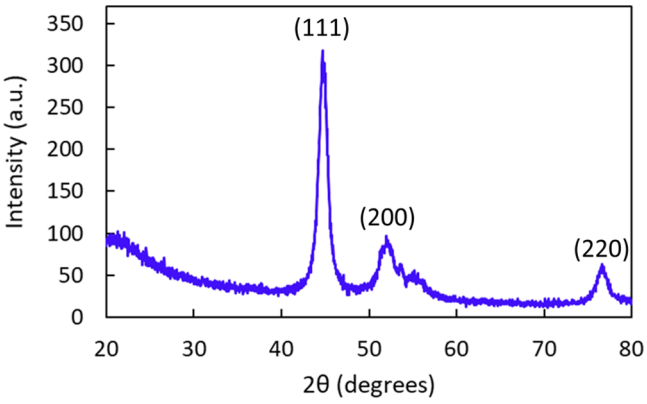

Figure 3. GI-XRD scan of the nickel film showing that the nickel film has a face-centered cubic crystal structure.

scan with the peaks referenced according to the literature.[39] These nickel films had a thickness of 165 Å with 18 Å native NiO according to X-ray reflectometry (XRR) analysis. Both GI-XRD and XRR scans were performed using a Bede D1 X-ray diffractometer from Jordan Valley Semiconductors with radiation from Cu Kα (λ = 1.540 Å). The X-ray tube filament voltage was 40 kV, and the current was 35 mA. The incident angle used for GI-XRD was 0.3°. The XRR scan range was 300−6000 arcsec with a 5 arcsec step size. The modeling software for the XRR scans was REFS, from Jordan Valley Semiconductors.

The nickel wafer was cut into 2 × 2 cm pieces to fit in the reactor. Thermal ALE experiments were performed with a SO_2Cl_2 and PMe_3 reaction sequence of 1-60-1-60. This timing sequence signifies a SO_2Cl_2 exposure of 1 s, followed by a 60 s Ar purge and then a PMe_3 exposure of 1 s, followed by a 60 s Ar purge. The nickel and NiO thicknesses after the ALE process were measured with XRR. The comparison of the nickel thickness before and after ALE determined the etch rate.

Scanning electron microscopy (SEM) was used for surface morphology comparisons of the nickel films prepared using physical vapor deposition. A Hitachi SU3500 SEM was used with an accelerating voltage of 15 kV. Atomic force microscopy (AFM) was utilized to evaluate the surface of these same nickel films before and after ALE. These AFM measurements were performed with a Park NX10 AFM instrument using the non-contact mode. The scan rate was 0.6 Hz with an Olympus micro cantilever probe (OMCL-AC160TS). The average RMS roughness values were obtained using RMS roughness measurements at three different positions for each sample.

2.3. Quadrupole Mass Spectrometry Experiments. Detection of volatile etch species was accomplished using a flange-mounted quadrupole mass spectrometer (Extrel).[40] The quadrupole mass spectrometer has 19 mm-diameter mass filter quadrupole poles, an operating frequency of 880 kHz, and a mass range of 1−1000 amu. Quadrupole mass spectrometry (QMS) acquisitions were performed in a mass-to-charge (m/z) window of 1−1000 amu using an electron ionization energy of 70 eV. QMS scans were recorded throughout the temperature ramp during experiments. Each scan from 1−1000 amu was completed in 2.20 s, and there were 27 data points per amu.

During the QMS experiments, ~0.5 Torr PMe_3 in N_2 carrier gas flowed through $NiCl_2$ powder (Strem Chemicals, 99.99+%).[40] A fraction of the N_2 carrier gas, etching products, and remaining PMe_3 precursor exits the sample holder through an aperture. Gas expansion through the aperture then creates a molecular beam that travels through a skimmer before arriving to the ionization region of the mass spectrometer.[40] Ionization of gas is achieved by electron-impact ionization with a circular thoriated iridium filament in the ionization volume. The QMS mass analyzer was positioned perpendicular to the incoming molecular beam to minimize exposures to corrosive gaseous species.

3. RESULTS AND DISCUSSION

3.1. QCM Measurements. QCM results during thermal ALE using SO_2Cl_2 and PMe_3 as the reactants on the nickel QCM at various temperatures are shown in Figure 4. The

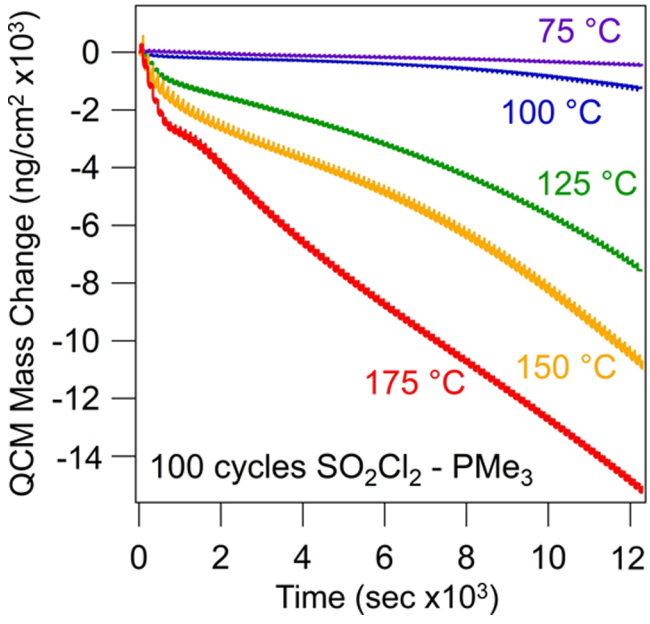

Figure 4. QCM mass change vs time showing 100 ALE cycles at 75, 100, 125, 150, and 175 °C.

lowest effective temperature for nickel ALE is 75 °C. At 50 °C, there is no etching using these reactants. Figure 4 reveals that the etch rate of the nickel film increases with increasing temperature. The steady-state etch rates in Figure 4 are 4.5, 17.8, 70.3, 135.3, and 175.3 ng/(cm^2 cycle) for the temperatures 75, 100, 125, 150, and 175 °C, respectively. The steady-state etch rates in ng/(cm^2 cycle) are equivalent to 0.05, 0.20, 0.79, 1.52, and 1.97 Å/cycle for the temperatures 75, 100, 125, 150, and 175 °C, respectively. These etch rates

https://doi.org/10.1021/acs.chemmater.1c02684
Chem. Mater. 2021, 33, 9174−9183

were determined using the conversion factor 1 Å Ni/cm^2 = 89.0 ng Ni/cm^2 based on a Ni density of 8.90 g/cm^3.

The first 15 ALE cycles in Figure 4 for each temperature do not show the same etch rates as the etch rates observed at later times. These differences are attributed to an oxide on the Ni surface that forms while the QCM equilibrates to a new temperature. An equilibration period of 12 h is required when changing between different temperatures. The nickel surface is prone to slow oxidation resulting from trace levels of H_2O or O_2 in the vacuum chamber during this equilibrium period. When the experiment begins at the new temperature, 10−15 ALE cycles are required to remove the thin surface oxide before reaching the new steady-state behavior.

The individual mass changes recorded using the QCM can be examined to understand the mechanism of Ni ALE. Figure 5 shows an expanded section for three Ni ALE cycles from the

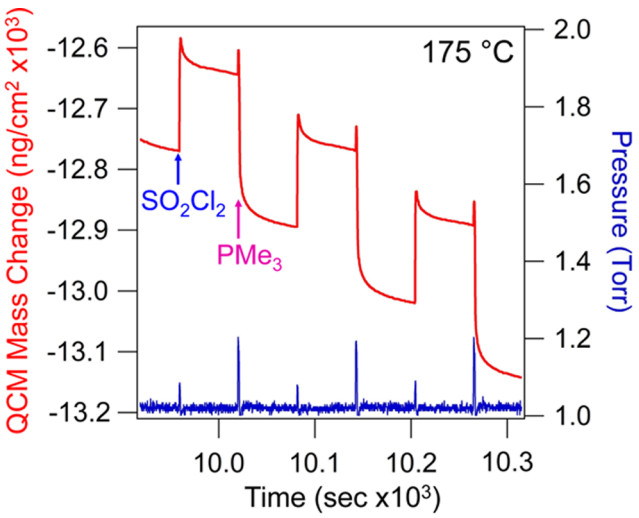

Figure 5. QCM mass change over three cycles of ALE using SO_2Cl_2 and PMe_3 at 175 °C.

QCM results at 175 °C in Figure 4. The mass increases during each SO_2Cl_2 exposure. This mass increase is consistent with adding Cl to the nickel surface to form $NiCl_2$ as shown in Figure 1. In contrast, the mass decreases during each PMe_3 exposure. The mass decreases to below the mass before the SO_2Cl_2 exposure. This mass decrease is consistent with the removal of the nickel by ligand addition as illustrated in Figure 1.

The magnitude of the mass change during each step of nickel ALE depends on temperature. Figure 6 shows two representative ALE cycles at temperatures of 75, 125, and 175 °C. These ALE cycles are taken from the QCM results shown in Figure 4. At each temperature, the reactant pressures were 100 mTorr for SO_2Cl_2 and 300 mTorr for PMe_3. In addition, the reactant exposure times were 1 s. These results indicate that the chlorine added during the SO_2Cl_2 exposure increases with temperature. Additionally, the mass lost during the PMe_3 ligand-addition step also increases with temperature. The combination of these two steps results in a net mass loss that increases with temperature.

At 175 °C, there is a slight decrease in mass after the SO_2Cl_2 exposure. This mass decrease may be the result of SO_2Cl_2 precursor desorption from the chlorinated $NiCl_2$ surface or newly formed $NiCl_2$ reacting with PMe_3 remaining on the surface from the previous PMe_3 exposure. In contrast, there is

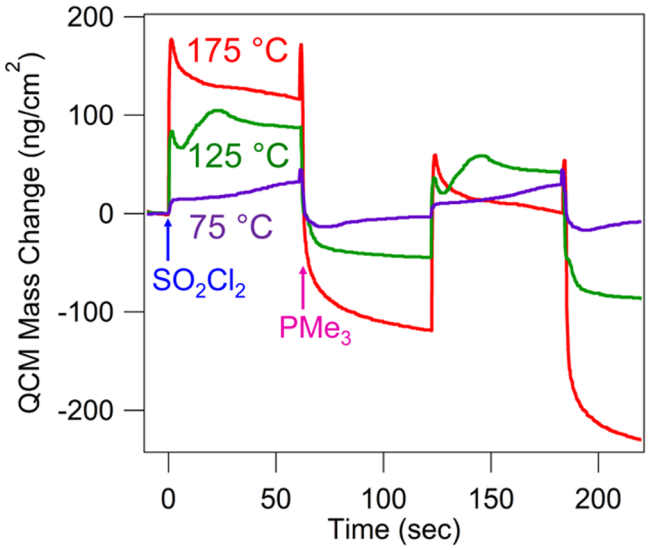

Figure 6. Comparison of QCM mass change over two cycles of ALE using SO_2Cl_2 and PMe_3 at 75, 125, and 175 °C.

an increase in mass after SO_2Cl_2 exposure at 125 and 75 °C. This mass increase is attributed to SO_2Cl_2 desorption from the chamber walls and continuous formation of $NiCl_2$ on the surface. At lower temperatures, SO_2Cl_2 requires more time to desorb and exit the chamber.

The QCM measurements can be used to determine how much $NiCl_2$ is created on each SO_2Cl_2 exposure and how much of this $NiCl_2$ is lost on each PMe_3 exposure. The nickel chlorination is analyzed assuming that all the mass gained during the SO_2Cl_2 exposure is chlorine. In addition, this chlorine is presumed to react with nickel to form stoichiometric $NiCl_2$. Finally, the surface area of the nickel QCM crystal is assumed to be 1 cm^2. This assumption is valid if the nickel film is smooth and if any possible roughness adds a negligible amount to the surface area.

For the first ALE cycle at 175 °C in Figure 6, the mass gained on the SO_2Cl_2 exposure is Δm = 128.59 ng/cm^2. Because the area of the available nickel film is 1 cm^2, the total mass gained on the QCM crystal is 128.59 ng. This mass gain represents the addition of 128.59 ng of Cl. This mass gain of chlorine is equivalent to the creation of 1.814×10^{-9} mol of $NiCl_2$ based on the molar ratio of 2 Cl to 1 $NiCl_2$. The mass of $NiCl_2$ formed is 235.05 ng using the molar mass of 129.6 g/mol for $NiCl_2$. The accepted density of $NiCl_2$ is 3.55 g/cm^3.[41] This density is then used to convert the mass of $NiCl_2$ to a $NiCl_2$ thickness of 6.62 Å. Because there is a large volume expansion during chlorination, this 6.62 Å of $NiCl_2$ was derived from 1.20 Å of metallic nickel.

The mass change on the PMe_3 exposure is Δm = −234.41 ng/cm^2 for the first ALE cycle at 175 °C in Figure 6. In comparison, there was 235.05 ng of $NiCl_2$ created from the SO_2Cl_2 exposure as determined previously. The remaining $NiCl_2$ left after the PMe_3 exposure is 235.05 ng − 234.41 ng = 0.64 ng. This amount is minimal. These results indicate that the PMe_3 ligand-addition step removes nearly all the $NiCl_2$ formed from the previous SO_2Cl_2 exposure on the QCM surface at 175 °C. In terms of film thicknesses, this one PMe_3 exposure resulted in the removal of 6.62 Å of $NiCl_2$ or 1.20 Å of the original metallic nickel.

The same process detailed above can be followed for the ALE cycles at the lower temperatures of 125 and 75 °C in

https://doi.org/10.1021/acs.chemmater.1c02684
Chem. Mater. 2021, 33, 9174−9183

Figure 6. This analysis reveals that not all the $NiCl_2$ is removed at lower temperature. At 125 °C, the mass gain resulting from the SO_2Cl_2 exposure is Δm = 96.29 ng/cm^2. In addition, the mass loss resulting from the PMe_3 exposure is Δm = −138.78 ng/cm^2. These mass changes result in a total of 37.23 ng of $NiCl_2$ left on the QCM after the ligand-addition step. This amount of $NiCl_2$ is 21.2% of the total $NiCl_2$ formed by the SO_2Cl_2 exposure on Ni at 125 °C.

At 75 °C, the mass gain resulting from the SO_2Cl_2 exposure is Δm = 18.77 ng/cm^2. In addition, the mass loss resulting from the PMe_3 exposure is Δm = −25.07 ng/cm^2. These mass changes result in a total of 9.24 ng of $NiCl_2$ left on the QCM after the ligand-addition step. This amount of $NiCl_2$ is 26.9% of the total $NiCl_2$ formed by the SO_2Cl_2 exposure on Ni at 75 °C. These results indicate that $NiCl_2$ builds up on the Ni surface at lower temperature. This buildup could result because of insufficient PMe_3 to remove all the $NiCl_2$. Alternatively, the desorption of the etch product may not be fast enough to prevent the etch products from blocking the remaining $NiCl_2$.

The chlorination of nickel by SO_2Cl_2 exposure was also investigated to characterize the self-limiting behavior. Figure 7

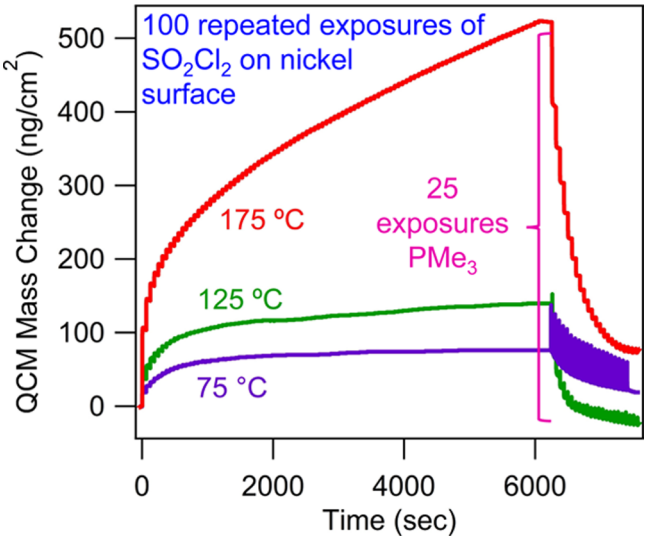

Figure 7. Comparison of QCM mass change during 100 exposures of SO_2Cl_2 followed by 25 exposures of PMe_3 at 75, 125, and 175 °C.

shows the results for 100 exposures of SO_2Cl_2 on a nickel surface at 75, 125, and 175 °C. At the lower temperatures of 75 and 125 °C, the chlorination is fairly self-limiting. In contrast, the chlorination is not self-limiting at 175 °C. Linear growth of the chloride is observed during the first few SO_2Cl_2 exposures. Subsequently, a diffusion-limited regime begins after about 20 SO_2Cl_2 exposures.

The progressive decrease in the chlorination rate is similar to the self-limiting behavior described by the Deal−Grove model when a growing surface layer acts as a diffusion barrier for reaction with the underlying layer.[42] This behavior has been observed in many other systems including the oxidation of silicon[42] and the fluorination of Al_2O_3.[10] According to free energy (ΔG) calculations for the chlorination of nickel to nickel (II) chloride using SO_2Cl_2, the ΔG becomes more negative as temperature increases.[29] The higher chlorination at a higher temperature of 175 °C is consistent with this thermochemical expectation. Higher diffusion rates for chlorine into the nickel film at higher temperature could also lead to greater chlorination.

Figure 7 also shows the results for 25 exposures of PMe_3 after the 100 SO_2Cl_2 exposures. The repeated exposures of PMe_3 did not fully remove the thick $NiCl_2$ layer. At 175 °C, the total mass gained from the 100 exposures of SO_2Cl_2 resulted in a mass change of Δm = 524.71 ng/cm^2. This chlorine mass change produces a $NiCl_2$ mass of 959.12 ng and an equivalent $NiCl_2$ thickness of 27.02 Å. Subsequently, 47% of this $NiCl_2$ was removed with repeated PMe_3 exposures. The rest of the $NiCl_2$ remains on the Ni surface.

At 125 °C, the total mass gained from the 100 exposures of SO_2Cl_2 resulted in a mass change of Δm = 142.31 ng/cm^2. This chlorine mass change produces a $NiCl_2$ mass of 260.13 ng and an equivalent $NiCl_2$ thickness of 7.33 Å. Afterward, 63% of the $NiCl_2$ was removed by repeated PMe_3 exposures. A similar behavior was observed at 75 °C. The total mass gained from the 100 exposures of SO_2Cl_2 resulted in a mass change of Δm = 76.83 ng/cm^2. This chlorine mass change produces a $NiCl_2$ mass of 140.44 ng and an equivalent $NiCl_2$ thickness of 3.96 Å. Subsequently, 41% of the $NiCl_2$ was removed with the repeated PMe_3 exposures.

This incomplete removal of $NiCl_2$ after the larger SO_2Cl_2 exposures will affect the subsequent Ni ALE cycles. The $NiCl_2$ layer is expected to reduce the chlorination during the next SO_2Cl_2 exposure. The previous results in Figures 4−6 were performed with only one SO_2Cl_2 exposure. Although the chlorination with SO_2Cl_2 is not in saturation, the amount of $NiCl_2$ removed by the subsequent PMe_3 exposure is almost complete at 175 °C. In contrast, the amount of $NiCl_2$ removal is not complete at the lower temperatures. These results argue that the optimum conditions for Ni ALE are at 175 °C with low SO_2Cl_2 exposures that are not self-limiting.

Repeated exposures of PMe_3 on bare nickel at 200 °C were also performed to determine if there was any spontaneous etching of nickel with only PMe_3 exposures. These experiments revealed that there was no mass loss after multiple PMe_3 exposures. There is no spontaneous etching of nickel by only PMe_3 exposures. Ni ALE requires both SO_2Cl_2 and PMe_3 exposures.

Figure 8 shows the average nickel etch rate determined from QCM measurements for each temperature. Six different nickel

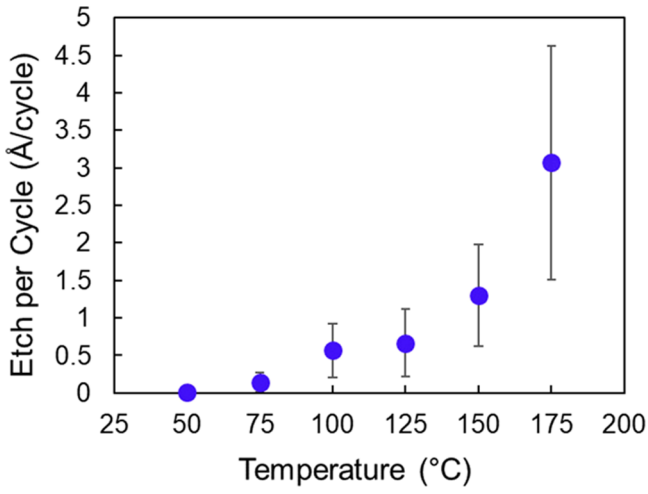

Figure 8. Average etch per cycle at various temperatures obtained from six different nickel QCM units.

https://doi.org/10.1021/acs.chemmater.1c02684
Chem. Mater. 2021, 33, 9174−9183

QCM units were etched over the course of this study. For each QCM unit, nickel was etched at multiple temperatures, and the average etch rate was determined at each temperature. The average etch rates were 0.14 ± 0.13, 0.57 ± 0.36, 0.67 ± 0.45, 1.30 ± 0.68, and 3.07 ± 1.56 Å/cycle for the temperatures 75, 100, 125, 150, and 175 °C, respectively. Although there is some variance in the etch rate between the different nickel QCM units, the nickel ALE is repeatable. Figure 8 also confirms that the nickel etch rate increases with temperature.

Another QCM study evaluated the constancy of Ni ALE over many ALE cycles. Figure 9 shows the results for one nickel QCM unit that recorded measurements for 1600 ALE cycles at 150 °C over the course of 8 days. Over this time, the entire nickel film with a thickness of ~200 nm was removed from the QCM monitor. The mass changes during the SO_2Cl_2 exposure and the PMe_3 exposure, as well as the total mass change, did not vary significantly with the etching of the nickel film.

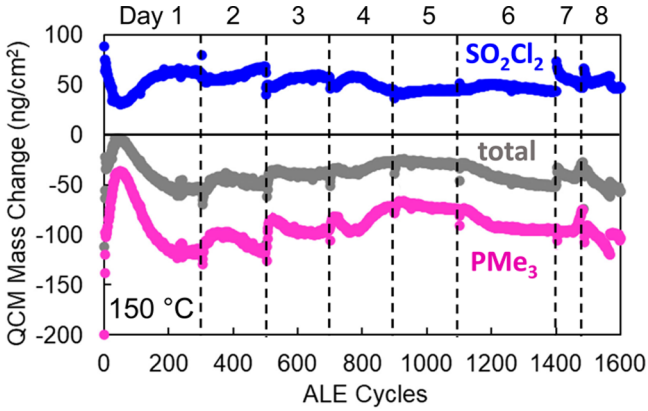

Figure 9. QCM mass change for each SO_2Cl_2 and PMe_3 half cycle and the total mass change per cycle at 150 °C on one QCM unit over 8 days.

The experiments in Figure 9 were performed using a new QCM unit that had been stored in air and had not been used for previous etching experiments. The etching during the first 200 cycles in Figure 9 displays the highest variation. This variation is attributed to the removal of the initial native oxide from the nickel surface. This passivating NiO layer is typically 10−20 Å thick, resulting from atmospheric exposure at room temperature.[43] Consequently, many ALE cycles are required to fully remove this native oxide.

After removing the native NiO film, the mass changes per ALE cycle are fairly consistent as the nickel film was etched progressively each day. The Ni film with an initial thickness of ~200 nm was completely removed by the 8th day. The results in Figure 9 indicate that the nickel film does not significantly roughen over the extended time required to perform 1600 ALE cycles. An increase in roughness would increase the surface area. The larger surface area would then cause an increase in the mass change per ALE cycle.

3.2. XRR, SEM, and AFM Measurements. The nickel etch rate has also been quantified on nickel thin films prepared using physical vapor deposition on thermal SiO_2 on a silicon substrate. Figure 10 shows the nickel film thickness as a function of the number of ALE cycles at 125, 150, and 200 °C. Each point on the graph corresponds to a new nickel coupon that has been etched for the desired number of ALE cycles.

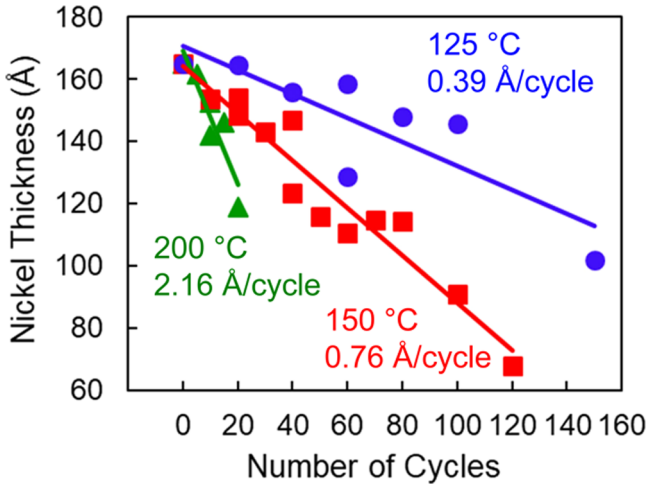

Figure 10. Nickel thickness vs number of ALE cycles showing the nickel coupon etch behavior at 125, 150, and 200 °C.

There is some variance across different coupons. The etch rate is smallest at 0.39 ± 0.10 Å/cycle at 125 °C. The etch rate increases to 0.76 ± 0.06 Å/cycle at 150 °C. The etch rate is largest at 2.16 ± 0.47 Å/cycle at 200 °C.

The XRR measurements of etch rates in Figure 10 and the QCM measurements of etch rates in Figure 8 both show an increase in the etch rate with temperature. There is also reasonable agreement between the etch rates measured by XRR and QCM analysis within the experimental errors. At 125 °C, XRR measured an etch rate of 0.39 ± 0.10 Å/cycle and QCM measured an average etch rate of 0.67 ± 0.45 Å/cycle. At 150 °C, XRR measured an etch rate of 0.76 ± 0.06 Å/cycle and QCM measured an average etch rate of 1.30 ± 0.68 Å/cycle. Some of the difference between the etch rates measured by the QCM and XRR studies may be attributed to the different methods employed to deposit the nickel films used in the QCM and XRR studies.

Figure 11 shows SEM images of the nickel film surface before and after 100 ALE cycles at 125 °C. The SEM images in Figure 11a,b are nearly identical. There is no change in the surface morphology after removing 20 Å of nickel during the 100 ALE cycles at 125 °C. This consistent morphology was confirmed by AFM images recorded for the pristine nickel film and for the nickel film after 80 cycles of ALE at 125 °C.

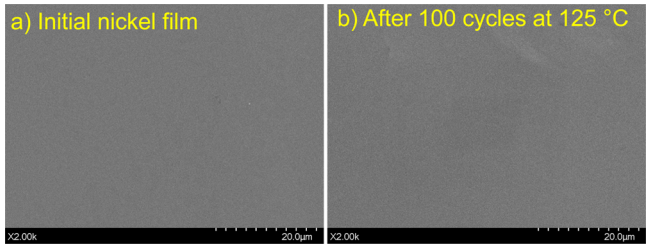

Figure 11. SEM images of (a) initial nickel film surface and (b) nickel film surface after 100 ALE cycles at 125 °C.

Figure 12a shows the AFM image of the initial pristine nickel film that has an RMS roughness of 0.55 nm. Figure 12b displays the AFM image of the nickel film after 80 Ni ALE cycles at 125 °C. This nickel film has a lower RMS roughness of 0.35 nm. In contrast, the AFM image in Figure 12c indicates that the nickel film after 100 ALE cycles has a larger RMS

https://doi.org/10.1021/acs.chemmater.1c02684
Chem. Mater. 2021, 33, 9174−9183

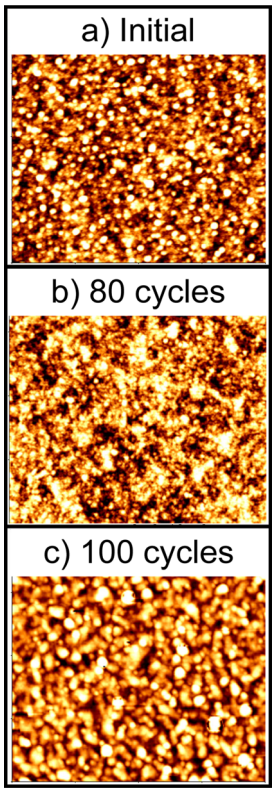

Figure 12. AFM images of (a) initial nickel film, (b) nickel film after 80 ALE cycles at 125 °C, and (c) nickel film after 100 ALE cycles at 125 °C.

roughness of 1.61 nm. This AFM image corresponds with the SEM image shown in Figure 11b. This increase in surface roughness observed using the AFM image is not apparent in the SEM image in Figure 11b.

The surface roughness of the nickel films was also determined using XRR measurements. The XRR analysis reveals that the RMS surface roughness is constant at 11−12 Å during the removal of the first 20 Å of the nickel film. For more ALE cycles, the XRR analysis monitors a slight increase in surface roughness. A comparison of the surface roughness determined using the AFM and XRR measurements is shown in Figure 13. There is a slight disagreement between the absolute surface roughness values. However, earlier comparisons of surface roughness determined using AFM and XRR measurements have also not been in exact agreement.[44,45] Both the AFM and XRR measurements record rougher surfaces after the removal of more than 20 Å from the initial Ni film. Similar results for the surface roughness were observed for Ni ALE at 150 °C.

The cause of the slight roughening of the nickel films after removal of more than 20 Å from the initial Ni film is not known. The QCM and XRR measurements do not support surface roughening versus ALE cycle. There is some curvature in the QCM measurements versus number of ALE cycles that could suggest a slightly increasing etch rate versus etching. This behavior could be interpreted as some roughening with etching. However, the results for the long 8 day etching experiment over 1600 ALE cycles at 150 °C shown in Figure 9 did not show a progressively larger etch rate with increasing number of ALE cycles.

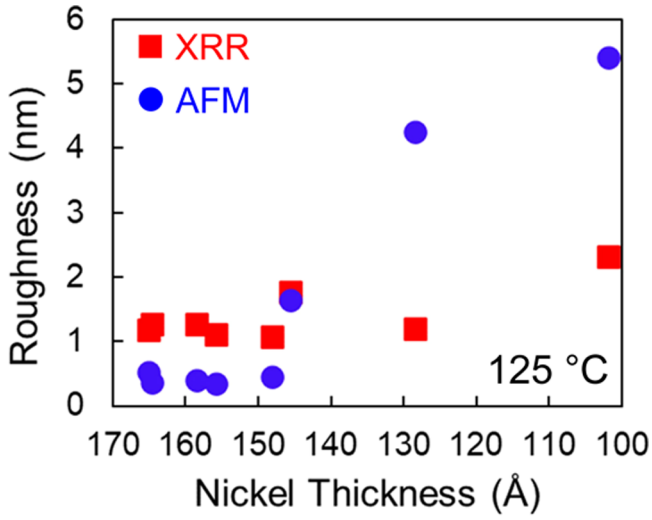

Figure 13. Average RMS roughness measured by AFM and XRR analysis for nickel film thicknesses after Ni ALE at 125 °C.

Another possibility is that there could be some delamination of the nickel films with an initial thickness of 165 Å, resulting from the etching process. The chlorination process during Ni ALE leads to a significant volume expansion. The expected volume expansion of x5.5 is based on a molar volume of Ni of 6.59 cm^3/mol and a molar volume of $NiCl_2$ of 36.5 cm^3/mol. This large volume expansion will lead to compressive stress in the $NiCl_2$ film. This compressive stress could promote film delamination.[46] In contrast, the QCM experiments were performed on much thicker Ni films with an initial thickness of ∼2000 Å that would be less susceptible to delamination.

3.3. QMS Studies. The mass loss observed by the QCM measurements indicates that volatile nickel species must desorb from the surface during the PMe_3 exposure. In situ QMS was utilized to identify the etch products leaving the surface. The MLX plot in Figure 2 indicates that $NiCl_2(PMe_3)_2$ or $NiCl_2(PMe_3)_3$ may be the likely etch products. For the QMS experiments, the PMe_3 reactant was flowed continuously through $NiCl_2$ powder. The $NiCl_2$ powder mimics the nickel surface after chlorination with SO_2Cl_2. This use of $NiCl_2$ powders maximizes the intensity of the etch products by increasing the sample surface area. There is also a continuous etch product signal because the $NiCl_2$ powder is effectively an infinite reservoir. The etch product can be produced until the depletion of the $NiCl_2$ powder.

Figure 14 shows QMS results at 82 °C for the m/z window from 270−300 amu. The major etch product, $NiCl_2(PMe_3)_2$, is observed in this window. The etch product can be identified based on the Ni and Cl isotopic abundances. The calculated isotopic fingerprints for $NiCl_2(PMe_3)_2$ are indicated by the blue lines. There is excellent agreement between the mass spectrum and the calculated isotopic pattern. The etch product shows that two PMe_3 molecules are added to the metal center in $NiCl_2$. The $NiCl_2(PMe_3)_2$ complex can then desorb from the surface. The other likely product predicted by the MLX plot, $NiCl_2(PMe_3)_3$, was not observed in the QMS experiments. These results agree with literature accounts where $NiCl_2(PMe_3)_3$ is reported to lose one PMe_3 ligand at room temperature to yield $NiCl_2(PMe_3)_2$.[47,48] $NiCl_2(PMe_3)_2$ is more stable than $NiCl_2(PMe_3)_3$ at elevated temperature.

The QMS study also investigated the amount of volatile etch species observed at various temperatures of the $NiCl_2$ powder.

https://doi.org/10.1021/acs.chemmater.1c02684
Chem. Mater. 2021, 33, 9174−9183

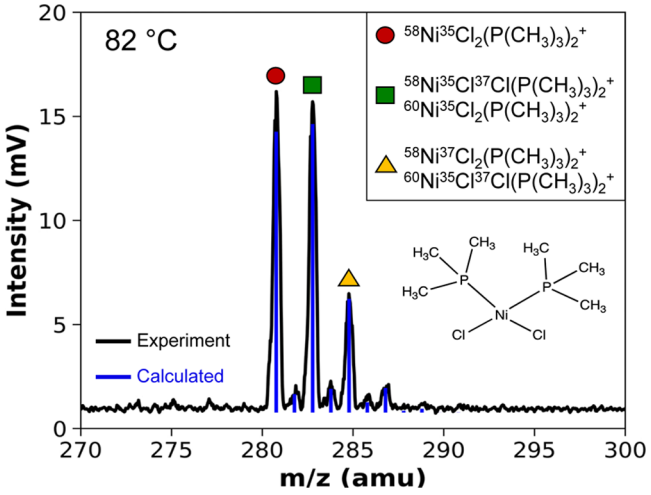

Figure 14. Mass spectrometry results for the nickel etch product, $NiCl_2(PMe_3)_2$, from the reaction of PMe_3 with $NiCl_2$ powder at 82 °C. The calculated isotopic spectrum and experimental spectrum agree very well.

Figure 15 shows a temperature ramp from room temperature to 200 °C. During the heat ramp, PMe_3 was continuously

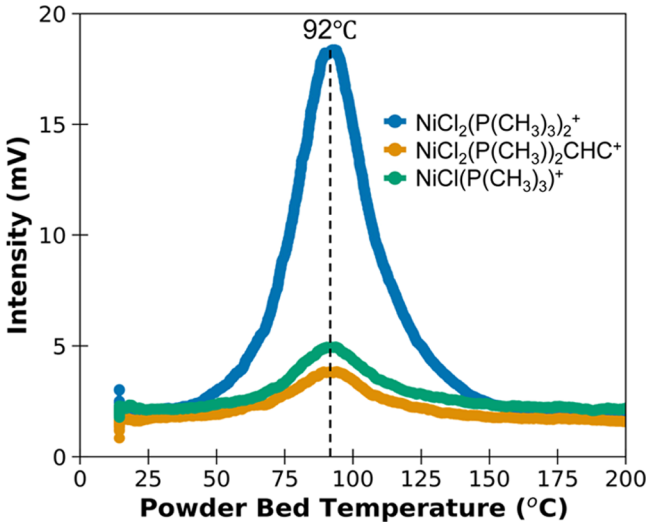

Figure 15. Mass spectrometry results for intensity of the nickel etch product, $NiCl_2(PMe_3)_2$, from the reaction of PMe_3 with $NiCl_2$ powder versus temperature from room temperature to 200 °C.

flowed through the $NiCl_2$ powder. The molecular ion of $NiCl_2(PMe_3)_2$ and its fragments were monitored as a function of temperature. The parent and fragments track each other, and all species peaked at 92 °C. This temperature peak at 92 °C may result from the decreasing residence time of the PMe_3 precursor and the increasing desorption rate of the $NiCl_2(PMe_3)_2$ product at higher temperatures.

The QMS results cannot be directly compared with the etching results from the QCM and nickel coupons. The QMS experiments use an infinite reservoir of $NiCl_2$ powder and only observe the PMe_3 ligand-addition reaction. The infinite reservoir of $NiCl_2$ may not be the same as the $NiCl_2$ created during the SO_2Cl_2 chlorination reaction. However, the QMS measurements observe $NiCl_2(PMe_3)_2$ in the same temperature range where mass loss is observed in the QCM experiments and Ni thickness reduction is monitored by the XRR measurements. The observation of Ni ALE together with the identification of $NiCl_2(PMe_3)_2$ as the etch product helps to confirm this approach using the CBC method to define metal thermal ALE processes.

4. CONCLUSIONS

A Ni thermal ALE process was demonstrated using chlorination and ligand-addition reactions. Chlorination of nickel was performed using SO_2Cl_2. Ligand addition was accomplished using PMe_3. QCM studies showed that nickel can be etched using this ALE mechanism from 75 to 175 °C. The Ni etch rate increased with increasing temperature. The average etch rates determined from the mass changes were 0.14 ± 0.13, 0.57 ± 0.36, 0.67 ± 0.45, 1.30 ± 0.68, and 3.07 ± 1.56 Å/cycle for the temperatures 75, 100, 125, 150, and 175 °C, respectively. XRR investigation monitored Ni etching from 125 to 200 °C. The etch rates measured by XRR analysis varied from 0.39 Å/cycle at 125 °C to 2.16 Å/cycle at 200 °C. Ligand addition of PMe_3 to $NiCl_2$ also resulted in $NiCl_2(PMe_3)_2$ as the volatile nickel-containing etch species. This species was identified by QMS studies, and its isotopic distribution confirmed the assignment as $NiCl_2(PMe_3)_2$.

The QCM studies allowed the mechanism of Ni ALE to be understood during the SO_2Cl_2 and PMe_3 exposures. The mass increased with each SO_2Cl_2 exposure as expected for the formation of $NiCl_2$. More $NiCl_2$ was formed at higher temperatures than at lower temperatures for a given SO_2Cl_2 exposure. In contrast, the PMe_3 exposure produced a mass reduction. The mass reduction was consistent with the volatilization of Ni-containing species resulting from the ligand-addition reaction. At lower temperature, the $NiCl_2$ builds up over many ALE cycles, resulting from the incomplete removal of $NiCl_2$ by PMe_3. The removal of $NiCl_2$ was more complete at higher temperatures. XRR and AFM studies also revealed that no surface roughness changes were observed until removal of more than 20 Å of the nickel film.

The inspiration of this chemistry for Ni ALE was the CBC method. The CBC method is a convenient way to determine the likely ligands on a metal based on known organometallic complexes. The MLX plots from the CBC method display the number of L and X ligands on the possible metal complexes. The sequential reactions during the metal ALE process can then be devised to produce these likely organometallic complexes. The $NiCl_2(PMe_3)_2$ product from the ligand addition of PMe_3 on $NiCl_2$ was consistent with the expectations from the MLX plots. The MLX plots should also be useful to define new thermal ALE processes for other metals.

AUTHOR INFORMATION

Corresponding Author

Steven M. George − *Department of Chemistry, University of Colorado, Boulder, Colorado 80309-0215, United States;* orcid.org/0000-0003-0253-9184; Email: Steven.George@Colorado.edu

Authors

Jessica A. Murdzek − *Department of Chemistry, University of Colorado, Boulder, Colorado 80309-0215, United States*

Ann Lii-Rosales − *Department of Chemistry, University of Colorado, Boulder, Colorado 80309-0215, United States*

Complete contact information is available at: https://pubs.acs.org/10.1021/acs.chemmater.1c02684

https://doi.org/10.1021/acs.chemmater.1c02684
Chem. Mater. 2021, 33, 9174−9183

Notes

The authors declare no competing financial interest.

■ ACKNOWLEDGMENTS

This research was funded by the Intel Corporation through a member-specific research project administered by the Semiconductor Research Corporation. The author thank their Intel Liaisons (Eric Mattson, Scott Clendenning, Charles Mokhtarzadeh, and Jiun-Ruey Chen) for useful discussions. The authors also acknowledge the Colorado Shared Instrumentation in Nanofabrication and Characterization (COSINC) facility for the SEM measurements. Additional support for the mass spectrometry experiments was provided by Lam Research.

■ REFERENCES

(1) Fischer, A.; Routzahn, A.; George, S. M.; Lill, T. Thermal Atomic Layer Etching: A Review. *J. Vac. Sci. Technol., A* **2021**, *39*, 030801.
(2) George, S. M. Mechanisms of Thermal Atomic Layer Etching. *Acc. Chem. Res.* **2020**, *53*, 1151−1160.
(3) Faraz, T.; Roozeboom, F.; Knoops, H. C. M.; Kessels, W. M. M. Atomic Layer Etching: What Can We Learn from Atomic Layer Deposition? *ECS J. Solid State Sci. Technol.* **2015**, *4*, N5023−N5032.
(4) George, S. M. Atomic Layer Deposition: An Overview. *Chem. Rev.* **2010**, *110*, 111−131.
(5) Lee, Y.; George, S. M. Thermal Atomic Layer Etching of Al_2O_3, HfO_2, and ZrO_2 Using Sequential Hydrogen Fluoride and Dimethylaluminum Chloride Exposures. *J. Phys. Chem. C* **2019**, *123*, 18455−18466.
(6) Zywotko, D. R.; Faguet, J.; George, S. M. Rapid Atomic Layer Etching of Al_2O_3 Using Sequential Exposures of Hydrogen Fluoride and Trimethylaluminum with No Purging. *J. Vac. Sci. Technol., A* **2018**, *36*, 061508.
(7) Kanarik, K. J.; Lill, T.; Hudson, E. A.; Sriraman, S.; Tan, S.; Marks, J.; Vahedi, V.; Gottscho, R. A. Overview of Atomic Layer Etching in the Semiconductor Industry. *J. Vac. Sci. Technol., A* **2015**, *33*, 020802.
(8) George, S. M.; Lee, Y. Prospects for Thermal Atomic Layer Etching Using Sequential, Self-Limiting Fluorination and Ligand-Exchange Reactions. *ACS Nano* **2016**, *10*, 4889−4894.
(9) Lee, Y.; George, S. M. Atomic Layer Etching of Al_2O_3 Using Sequential, Self-Limiting Thermal Reactions with $Sn(acac)_2$ and Hydrogen Fluoride. *ACS Nano* **2015**, *9*, 2061−2070.
(10) Cano, A. M.; Marquardt, A. E.; DuMont, J. W.; George, S. M. Effect of HF Pressure on Thermal Al_2O_3 Atomic Layer Etch Rates and Al_2O_3 Fluorination. *J. Phys. Chem. C* **2019**, *123*, 10346−10355.
(11) Gertsch, J. C.; Cano, A. M.; Bright, V. M.; George, S. M. SF_4 as the Fluorination Reactant for Al_2O_3 and VO_2 Thermal Atomic Layer Etching. *Chem. Mater.* **2019**, *31*, 3624−3635.
(12) Lee, Y.; DuMont, J. W.; George, S. M. Atomic Layer Etching of HfO_2 Using Sequential, Self-Limiting Thermal Reactions with $Sn(acac)_2$ and HF. *ECS J. Solid State Sci. Technol.* **2015**, *4*, N5013−N5022.
(13) Lee, Y.; DuMont, J. W.; George, S. M. Trimethylaluminum as the Metal Precursor for the Atomic Layer Etching of Al_2O_3 Using Sequential, Self-Limiting Thermal Reactions. *Chem. Mater.* **2016**, *28*, 2994−3003.
(14) Lee, Y.; George, S. M. Thermal Atomic Layer Etching of HfO_2 Using HF for Fluorination and $TiCl_4$ for Ligand-Exchange. *J. Vac. Sci. Technol., A* **2018**, *36*, 061504.
(15) Murdzek, J. A.; George, S. M. Effect of Crystallinity on Thermal Atomic Layer Etching of Hafnium Oxide, Zirconium Oxide, and Hafnium Zirconium Oxide. *J. Vac. Sci. Technol., A* **2020**, *38*, 022608.
(16) Murdzek, J. A.; Rajashekhar, A.; Makala, R. S.; George, S. M. Thermal Atomic Layer Etching of Amorphous and Crystalline Al_2O_3 Films. *J. Vac. Sci. Technol., A* **2021**, *39*, 042602.
(17) Myers, T. J.; Cano, A. M.; Lancaster, D. K.; Clancey, J. W.; George, S. M. Conversion Reactions in Atomic Layer Processing with Emphasis on ZnO Conversion to Al_2O_3 by Trimethylaluminum. *J. Vac. Sci. Technol., A* **2021**, *39*, 021001.
(18) DuMont, J. W.; Marquardt, A. E.; Cano, A. M.; George, S. M. Thermal Atomic Layer Etching of SiO_2 by a "Conversion-Etch" Mechanism Using Sequential Reactions of Trimethylaluminum and Hydrogen Fluoride. *ACS Appl. Mater. Interfaces* **2017**, *9*, 10296−10307.
(19) Johnson, N. R.; George, S. M. WO_3 and W Thermal Atomic Layer Etching Using "Conversion-Fluorination" and "Oxidation-Conversion-Fluorination" Mechanisms. *ACS Appl. Mater. Interfaces* **2017**, *9*, 34435−34447.
(20) Abdulagatov, A. I.; George, S. M. Thermal Atomic Layer Etching of Silicon Using O_2, HF, and $Al(CH_3)_3$ as the Reactants. *Chem. Mater.* **2018**, *30*, 8465−8475.
(21) Abdulagatov, A. I.; George, S. M. Thermal Atomic Layer Etching of Silicon Nitride Using an Oxidation and "Conversion Etch" Mechanism. *J. Vac. Sci. Technol., A* **2020**, *38*, 022607.
(22) Abdulagatov, A. I.; Sharma, V.; Murdzek, J. A.; Cavanagh, A. S.; George, S. M. Thermal Atomic Layer Etching of Germanium-Rich SiGe Using an Oxidation and "Conversion-Etch" Mechanism. *J. Vac. Sci. Technol., A* **2021**, *39*, 022602.
(23) Lee, Y.; George, S. M. Thermal Atomic Layer Etching of Titanium Nitride Using Sequential, Self-Limiting Reactions: Oxidation to TiO_2 and Fluorination to Volatile TiF_4. *Chem. Mater.* **2017**, *29*, 8202−8210.
(24) Konh, M.; He, C.; Lin, X.; Guo, X.; Pallem, V.; Opila, R. L.; Teplyakov, A. V.; Wang, Z.; Yuan, B. Molecular Mechanisms of Atomic Layer Etching of Cobalt with Sequential Exposure to Molecular Chlorine and Diketones. *J. Vac. Sci. Technol., A* **2019**, *37*, 021004.
(25) Mohimi, E.; Chu, X. I.; Trinh, B. B.; Babar, S.; Girolami, G. S.; Abelson, J. R. Thermal Atomic Layer Etching of Copper by Sequential Steps Involving Oxidation and Exposure to Hexafluoroacetylacetone. *ECS J. Solid State Sci. Technol.* **2018**, *7*, P491−P495.
(26) Xie, W.; Lemaire, P. C.; Parsons, G. N. Thermally Driven Self-Limiting Atomic Layer Etching of Metallic Tungsten Using WF_6 and O_2. *ACS Appl. Mater. Interfaces* **2018**, *10*, 9147−9154.
(27) Green, M. L. H. A New Approach to the Formal Classification of Covalent Compounds of the Elements. *J. Organomet. Chem.* **1995**, *500*, 127−148.
(28) Gupta, B. D. *Dictionary of Organometallic Compounds*, 2nd ed.; Chapman & Hall: London, 1995.
(29) *HSC Chemistry 9.9*; Outokumpu Research Oy: Pori, Finland.
(30) Williams, K. R.; Gupta, K.; Wasilik, M. Etch Rates for Micromachining Processing-Part II. *J. Microelectromech. Syst.* **2003**, *12*, 761−778.
(31) Tarn, P. W.; Walker, P. *CRC Handbook of Metal Etchants*; CRC: Boca Raton, FL, 1991.
(32) Cho, H. N.; Min, S. R.; Bae, H. J.; Lee, J. H.; Chung, C. W. High Density Plasma Etching of Nickel Thin Films Using a Cl_2/Ar Plasma. *J. Ind. Eng. Chem.* **2007**, *13*, 939−943.
(33) Matsui, N.; Mashimo, K.; Egami, A.; Konishi, A.; Okada, O.; Tsukada, T. Etching Characteristics of Magnetic Materials (Co, Fe, Ni) Using CO/NH_3 Gas Plasma for Hardening Mask Etching. *Vacuum* **2002**, *66*, 479−485.
(34) Kim, T.; Chen, J. K.-C.; Chang, J. P. Thermodynamic Assessment and Experimental Verification of Reactive Ion Etching of Magnetic Metal Elements. *J. Vac. Sci. Technol., A* **2014**, *32*, 041305.
(35) Sang, X.; Chang, J. P. Patterning Nickel for Extreme Ultraviolet Lithography Mask Application. II. Hybrid Reactive Ion Etch and Atomic Layer Etch Processing. *J. Vac. Sci. Technol., A* **2020**, *38*, 042604.
(36) Sang, X.; Chen, E.; Chang, J. P. Patterning Nickel for Extreme Ultraviolet Lithography Mask Application I. Atomic Layer Etch Processing. *J. Vac. Sci. Technol., A* **2020**, *38*, 042603.

https://doi.org/10.1021/acs.chemmater.1c02684
Chem. Mater. 2021, 33, 9174−9183

(37) Elam, J. W.; Groner, M. D.; George, S. M. Viscous Flow Reactor with Quartz Crystal Microbalance for Thin Film Growth by Atomic Layer Deposition. *Rev. Sci. Instrum.* **2002**, *73*, 2981−2987.
(38) Kharasch, M. S.; Brown, H. C. Chlorinations with Sulfuryl Chloride. I. The Peroxide-Catalyzed Chlorination of Hydrocarbons. *J. Am. Chem. Soc.* **1939**, *61*, 2142−2150.
(39) Joint Committee for Powder Diffraction Standards. *Powder Diffraction File No. 88-2326*; JCPDS International Center for Diffraction Data: Swarthmore, PA, 1998.
(40) Lii-Rosales, A.; Cavanagh, A. S.; Fischer, A.; Lill, T.; George, S. M. Spontaneous Etching of Metal Fluorides Using Ligand-Exchange Reactions: Landscape Revealed by Mass Spectrometry. *Chem. Mater.* **2021**, *33*, 7719−7730.
(41) Baxter, G. P.; Hilton, F. A. The Specific Gravity of Anhydrous Nickelous Chloride. The Determination of Specific Gravity by Displacement of Air. *J. Am. Chem. Soc.* **1923**, *45*, 700−702.
(42) Deal, B. E.; Grove, A. S. General Relationship for the Thermal Oxidation of Silicon. *J. Appl. Phys.* **1965**, *36*, 3770−3778.
(43) Graham, M. J.; Cohen, M. On the Mechanism of Low-Temperature Oxidation (23°−450°C) of Polycrystalline Nickel. *J. Electrochem. Soc.* **1972**, *119*, 879.
(44) Filies, O.; Böling, O.; Grewer, K.; Lekki, J.; Lekka, M.; Stachura, Z.; Cleff, B. Surface Roughness of Thin Layers - A Comparison of XRR and SFM Measurements. *Appl. Surf. Sci.* **1999**, *141*, 357−365.
(45) Su, H.-C.; Lee, C.-H.; Lin, M.-Z.; Huang, T.-W. A Comparison Between X-ray Reflectivity and Atomic Force Microscopy on the Characterization of a Surface Roughness. *Chin. J. Phys.* **2012**, *50*, 291−300.
(46) Thouless, M. D. Cracking and Delamination of Coatings. *J. Vac. Sci. Technol., A* **1991**, *9*, 2510−2515.
(47) Cao, R.; Wang, Q.; Sun, H. Dichloridotris(trimethylphosphine)nickel(II). *Acta Crystallogr., Sect. E: Struct. Rep. Online* **2008**, *64*, m335.
(48) Dawson, J. W.; McLennan, T. J.; Robinson, W.; Merle, A.; Dartiguenave, M.; Dartiguenave, Y.; Gray, H. B. Crystal and Molecular Structure of Dibromotris(trimethylphosphine)nickel(II). Electronic Structures and Stereochemistries of the Complexes $[NiX_2(PMe_3)_3]$. *J. Am. Chem. Soc.* **1974**, *96*, 4428−4435.

https://doi.org/10.1021/acs.chemmater.1c02684
Chem. Mater. 2021, 33, 9174−9183